

***Final Draft***  
**of the original manuscript:**

Fröbel, U.; Laipple, D.:

**On the formation of temperature-induced defects at the surface of TEM specimens prepared from TiAl using high-energy Gallium and low-energy Argon ions.**

In: Philosophical Magazine. Vol. 100 (2020) 15, 1915 - 1941.

First published online by Taylor & Francis: April 14, 2020

DOI: 10.1080/14786435.2020.1748245

<https://dx.doi.org/10.1080/14786435.2020.1748245>

# **On the formation of temperature induced defects at the surface of TEM specimens prepared from TiAl using high-energy Gallium and low-energy Argon ions**

Ulrich Froebel, Daniel Laipple

Helmholtz-Zentrum Geesthacht, Institute for Materials Research, Max-Planck-Straße 1, 21502 Geesthacht, Germany

Specimens for transmission electron microscopic (TEM) investigations were prepared from  $\gamma$  titanium aluminide alloys with Gallium and Argon ions using a focused ion beam (FIB) and a precision ion polishing system (PIPS). Preparation to electron transparency by Gallium ions alone leads to the formation of crystalline platelets of the  $\alpha$  titanium phase at the specimen surfaces, revealed through conventional and high resolution (HR) TEM analysis. The platelets are assumed to precipitate from priorly formed amorphous layers. The required crystallization temperature of about 480°C is generated through the ion bombardment implying that the  $\gamma$  titanium aluminides can be heated substantively during sputtering. The primary reason for this is the restricted transfer of heat away from the beam impact point when the specimen thickness comes close to the beam diameter. The formation of the platelets can be avoided by terminating the Gallium ion treatment prior to that, while providing for a sufficient thermal bonding of the specimen to the grid as well and polishing off the remaining material by Argon ions, which are much less focused and less energetic, so that the local heat peaks are reduced.

## **1. Introduction**

The focussed ion beam technique facilitates the targeted withdrawal of specimens from bulk material for TEM investigations [1]. In this process, however, the specimens experience various kinds of damage being confined to the surface regions or effecting the specimens as a whole [1, 2]. Amorphization and incorporation of beam ions are surface related damage whereas volume related damage might be caused by the heat produced during the ion beam bombardment depending on the actual temperature rises.

According to theoretical considerations, the temperature rises can be considerably when the specimens reach dimensions in the order of the ion beam diameter during the preparation process [3]. In the case of the TEM specimen preparation regarded here, this applies to the specimen thickness. The temperature increase is then attributed to the limited heat transfer from the beam impact point [3].

Such substantial temperature rises were in fact deduced from surface defect structures that were formed on a specimen of a  $\gamma$  titanium aluminide alloy during the preparation with Ga ions. The structures, which were analysed with different TEM techniques, will be described and assessed explicitly in the first part of the study. As a consequence of these findings, a modified preparation approach was developed. It comprises the preparation of unfinished specimens by Ga ions, which are subsequently polished into finished, electron transparent specimens by Ar ions. These specimens exhibit no structural evidences for elevated processing temperatures anymore. The associated technique will be described in the second part of the study. Prior to this, however, some background information on shear bands, from which the TEM specimens

were extracted, and on  $\gamma$  titanium aluminides in general will be provided in the following experimental section.

## 2. Specimen material and experimental details

Two-phase  $\gamma$  titanium aluminides are used in some high temperature aero-engine applications because of their low density and high structural stability. Of particular interest are the so-called high Nb-containing alloys within the base-composition range Ti-(44-47)Al-(5-8)Nb (in at %) [4, 5] standing out due to high attainable strengths and sufficient ductilities. The alloys mainly consist of the intermetallic phases  $\gamma$ (TiAl) with L1<sub>0</sub> structure and  $\alpha_2$ (Ti<sub>3</sub>Al) with D0<sub>19</sub> structure, where the volume fraction of the  $\alpha_2$  phase is between 5 and 20%. The atomic arrangements of the phases are depicted in Figure 1 together with the Burgers vectors of the  $\gamma$  phase.

The microstructures are relatively coarse after casting, mainly consisting of large lamellar colonies that are composed of  $\gamma$  and  $\alpha_2$  platelets and a small number of  $\gamma$  grains [6]. Such coarse and inhomogeneous microstructures are particularly harmful to the intrinsically brittle alloys, because high constraint stresses can develop after very small deformation strains and generate cracks. The microstructures must therefore become finer and more homogeneous, which can usually be achieved most effectively through hot-working by means of deformation-induced recrystallization processes. Such efforts are however impeded by the liability of the alloys to shear localization. In an attempt to elucidate the underlying mechanisms, high strain torsion tests were performed in order to obtain pronounced shear bands that show the characteristic features clearly [6, 7]. An example of such an experiment is given in Figure 2.

The lamellar structure is formed after casting in the course of the cooling process through the precipitation of the  $\gamma$  phase from the  $\alpha$  phase [8, 9]. The  $\alpha$  phase with A3 structure is the disordered variant of the  $\alpha_2$  phase. The transformation is finished when the eutectoid temperature is reached, which amounts to about 1120°C, depending on composition below which the  $\alpha$  phase converts into the  $\alpha_2$  phase. The resulting  $\gamma$  and  $\alpha_2$  platelets are crystallographically aligned according to the Blackburn relation [10]:

$$\{111\}_\gamma \parallel (0001)_{\alpha_2} \text{ and } \langle \bar{1}10 \rangle_\gamma \parallel \langle \bar{1}2\bar{1}0 \rangle_{\alpha_2}. \quad (1)$$

The planes and directions are illustrated in Figure 1. The disorder/order transformation of the  $\alpha$  phase into the  $\alpha_2$  phase leaves the crystal orientation unchanged, so that the Blackburn relation (1) is valid also for  $\gamma/\alpha$  interfaces. This mutual crystallographic orientation appears whenever one phase transforms into the other or when one phase evolves at the interface of the other. A second example for a phase transformation is the recrystallization of  $\alpha_2$  grains at the intersection zones of twins within a  $\gamma$  grain during hot-working [7], whereas the epitaxial growth of the  $\alpha$  phase on the  $\gamma$  phase will play a prominent role in the following section when interpreting the ion-induced defect structures.

The specimen preparation with Ga ions was conducted on the Zeiss FIB scanning electron microscope (SEM) cross-beam Auriga 60 instrument using two different ablation modes. These are the mill-for-depth treatment, where the material is removed line by line and layer by layer down to a predefined depth, and the deposition treatment, where the material is removed uniformly for a predefined time. The Gatan Model 691 PIPS instrument was used for the polishing with Ar ions.

The microstructural investigations of the shear zones (Figure 2) were performed with the SEM Leo Gemini 1530 using samples which were prepared by grinding and vibratory polishing (Vibromet 2 from the Buehler Corp.). The TEM specimens were examined using the electron microscopes PHILIPS CM 200 and FEI Titan 80-300 operated at 200kV and 300kV respectively, with the Titan being equipped with an energy dispersive X-ray (EDX) system from EDAX Inc. For image recording at the CM 200, negatives as well as image plates from the DITABIS Corp. were utilized. The image plates are more sensitive with regard to electrons than negatives therefore enabling considerably shorter exposure times advantageous for dark-field weak-beam (DF-WB) image recordings. Finally, diffraction patterns of zone axes were calculated to identify the phase constituting the damage layers using the SingleCrystal 3.1 software from CrystalMaker Software Limited.

### 3. Specimen preparation with Ga ions

Figure 3 shows the specimen which was prepared solely by Ga ions. The specimen was extracted from a shear band by means of a 30kV10nA beam along with a standard lift-out technique and then attached on one side with Pt to a commercially available Cu grid. At this stage the specimen thickness amounted to 2300nm approximately. The specimen was subsequently polished parallel to the grid surfaces from both sides uniformly down to a thickness of 200nm and 80nm by 30kV200pA and 30kV50pA beams respectively, using the mill-for-depth-mode.

The  $\gamma$  grain, which is marked in Figure 3 by arrow 1, was examined extensively with respect to the beam-induced damage in place of the rest of the specimen, which shows the very same damage throughout. The manifestations of the damage are illustrated consecutively. Figures 4a) and 4b) show the grain in  $[101]\gamma$  orientation and the associated diffraction pattern respectively. In addition to the spots constituting the  $[101]\gamma$  zone axis pattern (Figure 4b)) further spots may appear when changing the selected area diffraction (SAD) aperture diameter or position, so that at least four different diffraction patterns can be distinguished from each other. Accordingly, Figure 4c) indicates the pattern when using a big SAD aperture. The additional spots are arranged alongside or parallel to both  $g\{111\}\gamma$  reciprocal lattice vectors. When using a small aperture the patterns of Figure 4d) and 4e) might be obtained. The additional spots are then arranged exclusively alongside or parallel to the one or the other of the two  $g\{111\}\gamma$  reciprocal lattice vectors so that two different variants 1 (Figure 4d)) and 2 (Figure 4e)) result. The superposition of the two variants leads to the pattern of Figure 4c).

The variants 1 and 2 can be allocated to clearly discriminable areas when imaging the grain under two different diffraction conditions using BF as well as DF techniques (Figures 4f) to 4i). The edge of such an area is depicted in the HRTEM image of Figure 5, which was recorded in the thinnest region of the specimen being marked in Figure 3 with arrow 2. It indicates a Moiré pattern thereby revealing that the areas are platelets of crystalline structure situated on the two surfaces of the grain and are not any defects that are located within the base material. This view is supported by the stereographic recording shown in Figure 6. There are many dislocations visible in the left part of the grain. At first glance, some of the dislocations seem to be decorated by impurities in accordance with the extensive dark-appearing regions (arrow). However, a closer inspection reveals that the dark regions are flat and streaky as well as located at the surfaces so that they must be manifestations of the Moiré contrast generated by the crystal platelets. It is also worth mentioning that the diffraction contrast appears speckled.

The diffraction patterns of Figures 4c) to 4e) have been formed by spots that arose either from single diffractions, where the incident beam is diffracted solely at the specimen or a crystal platelet, or from double diffractions, where the beam is diffracted at the specimen and once again at a crystal platelet or vice versa [11]. Accordingly, the platelets contribute to the diffraction patterns in a complex fashion so that comprehensive crystallographic data is required to be able to identify the phase of the platelets. To this end, the  $\gamma$  grain was tilted in additional zone axes (Figure 7). This made it possible to recognize the platelet phase as  $\alpha$  titanium, which will be rendered reasonable in the following.

The diffraction patterns of the  $[011]\gamma$  and  $[110]\gamma$  zone axes are depicted in Figure 8. The  $[011]\gamma$  patterns (Figures 8a) to 8c)) are identically equal to the corresponding  $[101]\gamma$  patterns (Figures 4c) to 4e)). However, the two variants are now termed variant 2 (Figure 8b)) and variant 3 (Figure 8c)), which will become evident below. Of different appearance are the patterns of the  $[110]\gamma$  zone axis (Figures 8d) to 8f)). The additional spots of the variant 1 (Figure 8e)) and variant 3 (Figure 8f)) are again arranged exclusively alongside or parallel to one  $g\{111\}\gamma$  reciprocal lattice vector. Yet, the density of the spots is twice the density of the corresponding  $[101]\gamma$  and  $[011]\gamma$  spots in accordance with the additional superlattice spots of the  $[110]\gamma$  zone axis along  $g(001)\gamma$  (compare Figures 4b) or 8a) with 8d)). Furthermore, the pattern of Figure 8d) cannot be formed by simply superposing the variants 1 and 3 patterns, because additional spots appear, which do not belong to one or the other variant.

The diverse observations can be explained when constructing certain diffraction patterns of the  $[101]\gamma$  and  $[110]\gamma$  zone axes by overlaying the diffraction patterns of the  $\gamma$  and  $\alpha$  phase crystals (Figure 9) that were calculated regarding the mutual orientation relationship stated in equation 1. This very relationship, namely, allows a variety of crystallographically equivalent orientations of the platelets with respect to  $\gamma$  in accordance with the crystal symmetry of the  $\gamma$  phase. In particular, the  $(0002)\alpha$  plane of the platelets can be aligned parallel to one of the four  $\{111\}\gamma$  planes (Figure 10), which is reflected in the coincidence of the reciprocal lattice vector  $g(0002)\alpha$  with always one reciprocal lattice vector  $g\{111\}\gamma$  (Figure 9). The related variants 1, 2, or 3 then arise as a result of various double and threefold diffractions (Figures 9b) to 9d)).

Finally, the fourth variant (Figure 10) was detected along the  $[111]\gamma$  zone axis (Figure 11a)) while the variants 2 and 1 were additionally detected along the  $[112]\gamma$  and  $[211]\gamma$  zone axes (Figures 11b) and 11c)) for consistency checking purposes. There is a considerable misfit along these zone axes between the  $\gamma$  and  $\alpha$  phases which amounts, for instance, to about plus 4.4% or plus 3.4% for the  $\alpha$  phase alongside  $g(\bar{1}\bar{1}20)\alpha$  (Figure 11b) or Figure 11c)). Nevertheless, the corresponding  $\gamma$  and  $\alpha$  spots coincide well so that a substantial part of the misfit must be accommodated elastically by the  $\alpha$  phase. In accordance with theoretical considerations [12] such high elastic strains can only occur in very thin layers which are strongly bonded to the substrate. It is therefore assumed that the crystal platelets are merely a very small number of atomic planes thick. In this connection it is also noteworthy that the spots of the  $[101]\gamma$ ,  $[011]\gamma$ , and  $[110]\gamma$  zone axes are, in general, not exactly lined up along or parallel to the vectors  $g\{111\}\gamma$  but rather follow a zig-zag course, which becomes most obvious when considering the calculated double diffraction spots of Figures 9b) and 9c). The effect is pronounced for the  $[101]\gamma$  zone axis (Figure 9b)) and less noticeable for the  $[110]\gamma$  zone axis (Figure 9c)), owing to the tetragonality of the  $\gamma$  phase. The effect might be reduced further by elastic straining, with the zig-zag shaped course the less perceptible the thinner the platelets are. Furthermore, the strains lead to interfacial constraint stresses, which may naturally explain the deflection of the  $\gamma$  foil at the edge of the crystal platelet (Figure 5).

It is assumed that the crystal platelets evolve in a gradual manner. In the first instance, amorphous layers are formed at the specimen surfaces. The resulting interfaces are the nucleation sites for the platelets, which subsequently grow into the layers parallel and perpendicular to the interfaces. The details will be discussed below.

The kinetic energy and momentum of the Ga ions are transferred to the specimen by both inelastic and elastic interactions with the constituting atoms [2] which are situated within the penetration depth of the ions, thereby determining the layer thickness. The elastic interactions may displace atoms from their initial lattice sites, thereby creating defects such as interstitial-vacancy pairs, which finally can give rise to amorphization or remove surface atoms from the specimen surface and lead to sputtering. The atoms are removed with frequencies that vary from element to element so that different sputtering yields  $Y$  result for the alloying elements Al, Ti, and Nb, with  $Y$  being the average number of atoms that are ejected from the specimen per incident ion [13]. According to TRIM (transport of ions in matter) calculations [14], the sputtering yields for 30kV Ga beams and glancing-angle sputtering used here are 34.78, 13.28, and 10.31 regarding Al, Ti, and Nb, respectively [13]. Consequently, the surfaces become depleted with respect to Al, which is quantitatively expressed by the quotient  $c'_{Al}/c'_{Ti+Nb} = c_{Al} \cdot Y_{Ti+Nb} / (c_{Ti+Nb} \cdot Y_{Al})$  [15].  $c'_{Al}$  and  $c'_{Ti+Nb}$  are the steady-state concentration of Al and the summed up concentration of Ti and Nb during sputtering, whereas  $c_{Al}$  and  $c_{Ti+Nb}$  are the corresponding concentrations before sputtering, while  $Y_{Ti+Nb}$  denotes the weighted average sputter yield of Ti and Nb. The quotient  $c'_{Al}/c'_{Ti+Nb}$  amounts to 0.325, from which the Al concentration  $c'_{Al} = 24.5\%$  can be deduced, which is considerably smaller than the nominal concentration. It is, however, clearly above the expected concentration. In accordance with the phase diagram of the Ti-Al system [16], the maximal possible solubility of Al should be about 12% at intermediate temperatures where, to pre-empt implications of the subsequent discussion, the  $\alpha$  phase is formed. This discrepancy can be solved when considering that at such low temperatures the mobility of the atoms is limited substantially so that thermal equilibrium cannot be adjusted. It might further be anticipated that the solubility of Al is altered through the elastic straining of the  $\alpha$  phase to accommodate the  $\alpha/\gamma$  misfit.

Amorphization is expected especially for non-metallic materials like silicon, which have pronounced covalent binding characteristics in contrast to metals, since amorphization is usually ascribed to the directional nature of the covalent bindings, hampering the atomic rearrangements necessary to heal the defects created by the ion beam [2]. However, the  $\gamma$  phase has covalent binding shares [17] and thus also a certain propensity for amorphization. This was revealed by HRTEM investigations of a  $\gamma$  alloy, which was shot peened and showed amorphous structures within the heavily deformed surface layers [18]. The atomic rearrangements are additionally hampered by the unequal atomic sizes of the elemental constituents in metallic alloys [15] considered here. This effect is certainly further enhanced through elements which have been incorporated into the surface layer during the preparation process. First and foremost the element Ga must be mentioned here, whose content depends, according to theoretical considerations, on the incident angle of the ion beam and is smallest for glancing-angle sputtering used in the present study, with the concentrations being up to 10% [2]. Further elements might be Pt, which is present in the atmosphere of the working chamber of the FIB due to the sputtering of the Pt layer (Figure 3), as well as O and N, which are always present to some extent. In addition to such microstructural transformation processes redeposition might contribute to the formation of the amorphous layers, where sputtered material from the beam impact point is deposited in regions of the specimen lying in the flight path.

The thickness of the layer under glancing-angle sputtering conditions only depends on the

acceleration voltage and, of course, on the material being prepared [19]. For silicon a linear relationship between thickness and acceleration voltage was found, with the thickness being about 20 nm for a 30 kV beam [19] used for the present specimen preparation. When applying this value to  $\gamma$  titanium aluminium and considering the specimen thickness of 80 nm, one-half should be directly damaged by the ion bombardment. Such a big portion, however, cannot be deduced from the stereographic image of Figure 6 when closely inspecting the depicted dislocation structures. The dislocation lines, which are situated inclined to the specimen surface and hence terminating at the lower and upper specimen/layer interfaces, occupy at least nine-tenth of the overall specimen thickness implying a layer thickness of less than 4 nm.

When a layer thickness of 4 nm is assumed and it is also considered that Ga atoms are primarily incorporated into the outer-half of the layers [20], then an average Ga concentration of less than 0.5% results for the specimen in accordance with the above considerations. Such low concentrations are at or below the detection limit of EDX systems and may explain that Ga was difficult to detect at all.

Nevertheless, several percent of Ga might be present in the layers. Such low concentrations can probably be integrated into the  $\alpha$  phase considering the high solubility of this element in both the  $\gamma$  and  $\alpha_2$  phase and it exclusively occupying the Al lattice sites [21]. This might also be valid for the  $\alpha$  phase since the comparability of Al and Ga in the  $\gamma$  and  $\alpha_2$  phases must be ascribed to similar electron configurations as a result of their common affiliation to the third group of elements. Therefore it is understandable that no Ga specific phases have been formed. Also small amounts of Pt can be integrated into the  $\alpha$  phase in accordance with the associated solubility limit of about 0.25% [22].

The rearrangement of the atoms during the formation of the  $\alpha$  phase needs energy for the required diffusion processes, which is provided by the heat produced through the ablation process. Assuming the  $\alpha$  phase is not formed indirectly via the intermediate amorphous phase but directly from the  $\gamma$  phase, then the atoms remain permanently in the crystalline state, which lies energetically below the amorphous state, so that the driving force for diffusion is smaller for that reason alone. However, there is also the sluggish diffusion due to both the low mobility of the lattice atoms in  $\gamma$  titanium aluminides [23] in general, resulting from the ordered crystal structures as well as Nb, which is a slow diffuser in the  $\gamma$  phase [23], and the above mentioned mobility limitations at intermediate temperatures in particular. Consequently, the direct formation of the  $\alpha$  phase needs more energy than the indirect formation, implying that the necessary heating is higher. It appears also less likely, because the crystal structure becomes severely distorted through the Ga ion bombardment, so that it is questionable whether some kind of order can still be attributed to the compound at all. However, the direct formation of the  $\alpha$  phase from the  $\gamma$  phase cannot be ruled out definitely in accordance with the present observations.

According to the work from Banerjee et al. [24], who have investigated sputtered  $\gamma$  titanium layers heat-treated in-situ in the TEM up to the crystallization temperature, the energy necessary to maintain precipitation of the  $\alpha$  phase from the amorphous phase is attained just at intermediate temperatures. Microcrystalline agglomerates of the  $\alpha$  phase, which were formed during the sputtering process, start to grow into the amorphous matrix of a binary Ti-48Al alloy at 480°C. In connection with the preceding discussion about amorphization it is worth mentioning that no phase agglomerates were found in a quaternary Ti-48Al-2Mn-2Nb alloy after sputtering, which was attributed to the stabilizing effect of Mn and Nb onto the amorphous phase [24]. This effect should be even more pronounced in the alloy under consideration, when

taking into account the comparatively high Nb content so that the real crystallization temperature is quite probably above 480°C.

The detection of the crystal platelets is, in the light of the above considerations, an indirect proof that processing temperatures of more than 480°C are possible during focused ion beam sputtering of  $\gamma$  titanium aluminides. To the best of the author's knowledge no experimentally determined processing temperatures have been reported yet for this specimen preparation technique, not to mention such high temperatures. However, there are various theoretical investigations, which estimated the influence of the beam power  $P$ , specimen thermal conductivity  $\kappa$ , and specimen geometry on the resulting temperature increase. Accordingly, the temperature increase for a semi-infinite specimen with a flat surface is  $T=P/(a\cdot\pi\cdot\kappa)$  [25], with  $a$  being the radius of the ion beam when hitting the specimen surface. The thermal conductivity is approximately  $\kappa = 24.2\text{W}/(\text{m}\cdot\text{K})$  for  $\gamma$  titanium aluminides at room temperature [26]. As stated earlier, the specimen preparation was conducted successively with the beams 30kV10nA, 30kV200pA, and 30kV50pA in this very order, with the related beam radii being 0.5 $\mu\text{m}$ , 0.025 $\mu\text{m}$ , and 0.015 $\mu\text{m}$ , respectively. This results in  $P$  values of 0.0003, 0.000006, and 0.0000015W and temperature determining  $P/a$  values of 600, 240, and 100W/m. These beam conditions are in medium to low range when considering that values from 1000 down to 1W/m are available in commercial instruments [2]. The resulting temperature increases would be 7.9, 3.2 and 1.3°C, respectively, and thus negligibly small for a flat  $\gamma$  titanium aluminium specimen with large dimensions. This is because the transfer of heat from the beam incident point is very effective under such conditions [2].

However, the transfer of heat is limited considerably when the specimen reaches dimensions during the sputtering process that are in the order of the ion beam radius. In the case of the TEM specimen preparation considered here, this applies to the specimen thickness. Then temperature increments of up to several hundred °C are expected [3]. This is comprehensible when realizing that the energy input is extremely localized. It is assumed that the volume, which is heated up by the beam, is restricted to a hemisphere with a radius that is twice the beam radius [3]. Within this very volume the material is melted and moved off.

The estimates give valuable hints on how to proceed in order to reduce the processing temperatures distinctly, which is essential in order to minimize the temperature related specimen damage. Dislocation climb, for example, determines the deformation behaviour of  $\gamma$  titanium aluminides closely above 500°C [26] and commences, thus, near the temperatures that were present during the preparation process. It is therefore likely that the dislocations changed their configurations so that they are not representative any more for the bulk material from which the specimen was extracted.

The efforts must be targeted towards an improved heat transfer away from the ion beam incident point towards the grid. Therefore, the specimen thickness should always remain large when compared with the beam radius and, furthermore, a good thermal connection between the specimen and the grid should be ensured. In principle, the first objective can be reached by leaving the specimen thick or by making the beam radius small. Very small beam radii can be adjusted in modern focused ion beam instruments by choosing small beam energies and currents, which is usually used to minimize the thickness of the surface damage layers [27]. Yet, such beam conditions are impracticable for the preparation of comparatively large specimens because of the resulting small ablation rates or extensive preparation times. However, large specimens are beneficial when analysing dislocation or crystal structures,

because such investigations require distinct grain orientations, which with the tilt capabilities on hand are the more likely accessible the more grains are present.

A different approach was therefore chosen. It comprises, firstly, the preparation of a relatively thick specimen by focussed Ga ions of high energy and, secondly, the subsequent polishing to electron transparency by low energy Ar ions. Very small Ar ion beam energies are attainable, because Ar ions are lighter than Ga ions and since they are usable at quite low acceleration voltages, even when deploying an instrument that is not of the latest generation like the PIPS utilized in the present study. The low beam energies have the additional advantage that only thin damage layers are formed. Also rather small P/a values are attainable since the beams are much less focussed than the Ga ion beams. To be precise, the beam conditions used were 2kV, 5 $\mu$ A, and  $a = 0.0006\text{m}$  resulting in  $P = 0.01\text{W}$  and  $P/a = 16.7\text{W/m}$ . The P/a value is significantly smaller than the corresponding values adjusted during the FIB treatment. Thus the local heating is less serious. This was revealed by the direct measurement of temperature rises when preparing silicon specimens by Ar ions at various acceleration voltages, incident beam angles and beam currents. Accordingly, the temperature rise was only about 75°C when using an acceleration voltage of 5kV, a beam current of 1mA, and an incidence angle of 15° [28], that is, when using a higher beam energy and current than in the present study. In spite of the small P/a values the sputter yields are adequate owing to relatively large beam currents or beam powers.

#### **4. Specimen preparation with Ga and Ar ions**

The preparation procedure used is schematically depicted in Figure 12. It comprises the preparation of a half-grid (Figure 12a), the fixation of the specimen in the half-grid (Figure 12b), the subsequent thinning (Figure 12c), all with Ga ions, as well as the final polishing with Ar ions (Figure 12d).

It was necessary to prepare grids of a  $\gamma$  titanium aluminide alloy in order to ensure identical ablation rates during the final Ar polishing for both the grids and specimens. Conventional grids are often made of Cu. Cu, however, is less resistant to Ar ion bombardment than the  $\gamma$  titanium aluminides, leading to the destruction of the specimen connections from the side of the grid before the specimen is electron transparent. In contrast, a more resistant material might lead to the formation of protrusions on the grid resulting in a partial shadowing of the Ar beam and an irregular ablation of the specimen. The preparation of grids has the additional advantage that the design can be adjusted to personal needs. For dislocation analysis it is helpful to use half-grids with a diameter of 2.3 instead of 3 mm, because the related TEM holders are smaller in diameter, which allows higher tilting angles within the narrow gaps of the objective lens pole pieces. It is also beneficial that the specimens can be fixed exactly at the specimen centre so that the region of interest does not move from the visual field when tilting.

A good thermal coupling between the specimen and grid is achieved by producing connections along the entire cross-sections via redeposition processes (Figure 12b)). Such continuous connections are essential because sufficient thermal coupling must be maintained during the whole thinning and polishing process, no matter from where material is ultimately removed. They cannot be produced with the GIS using W or Pt, for example, because the deposition generated this way might form bridges in the narrow gaps between the grid and specimen during the early stages of the pinning process, thus subsequently shadowing the beam, so that the regions behind cannot be filled. Furthermore, W or Pt have ablation rates different from TiAl,

resulting in the same difficulties discussed in the preceding paragraph. In order to protect the connections during polishing, the specimen is thinned in such a way that it becomes broader towards the connections and beyond (Figure 12c)). The thinning occurs parallel to the grid. To this end, the specimen surfaces must be turned slightly into the beam to obtain parallel surfaces eventually. Otherwise, the specimen would become broader towards the lower regions, because the ablation decreases with increasing milling depth attributed to redeposition processes [29]. A second reason is the uneven sputtering caused by the features of the beam-profiles [30], which are characterized by a continuous decrease of the ion intensities towards the beam periphery thereby reducing the milling rates accordingly. Additionally, the grid was rotated during polishing in order to accomplish a uniform ablation and to minimize surface ripple formation, which is widespread during ion bombardment [31]. The rippling is attributed to the competition between smoothing by surface diffusion or viscous flow and, on the other hand, roughening due to local specimen curvatures, since the sputter yields depend on the angle of incidence. Finally, the grid-holder was specially designed in order to meet the needs required during polishing, with the protrusions (Figures 12d) and 13) intended to protect the connections against beam damage and reduce the processing temperatures due to sequentially blanked beams.

The various stages of the preparation procedure are illustrated by the SEM images depicted in Figure 14. The specimen, which is represented in Figure 14 f), was imaged using 6keV electrons. Under this imaging condition the central region appears bright and shows microstructural details when detecting secondary electrons. The imaging method is very helpful to identify the appropriate polishing times, because such regions are transparent for 200keV electrons, which is revealed by the TEM BF image depicted in Figure 15. The area is as wide as the area of the specimen, which was thinned by Ga ions alone (Figure 3). However, it is almost 4 times taller, which shows that quite large electron transparent areas can be prepared by this technique. The  $\gamma$  grain, whose position is marked in Figure 15 by an arrow, is represented in Figure 16 in two different crystallographic orientations (Figures 16 a) to 16d)). The first is the  $[101]\gamma$  orientation (Figures 16a and 16b)) and the second is the  $[110]\gamma$  orientation (Figures 16c and 16d)). The diffraction contrast of the grain (Figures 16a) and 16c)) appears much less speckled than the diffraction contrast of the grain showed in Figure 4a), which indicates that the surface damage is much less here than there. This observation is in agreement with the related diffraction patterns, which show no other spots but those belonging to the  $\gamma$  phase. Consequently, no crystal platelets were formed during the preparation with both Ga and Ar ions thereby also implying, that the related processing temperatures were low when compared with the ones that were present during the preparation with Ga ions alone.

The dislocation analysis (Figures 16e) and 16f)) took place starting from the  $[110]\gamma$  zone axis (Figures 16c) and 16d)). This approach has the advantage that superdislocations can easily be distinguished from ordinary dislocations, since the excitation with the reciprocal lattice vector  $g(001)\gamma$ , or multiples of it (Figure 16 d)), results in disappearing diffraction contrast, only for  $\frac{1}{2}\langle 1\bar{1}0 \rangle$  ordinary dislocations, in accordance with the cancellation rule. According to this, the Figures 16e) and 16f) show a mixture of ordinary dislocations and superdislocations or exclusively superdislocations, respectively. Obviously, the diffraction contrast of the dislocations is not superimposed by the diffraction contrast, resulting from surface defects of any kind, so that also the dissociation of the superdislocations into partial dislocations is clearly visible.

## 5. Conclusions

It has been shown that TEM specimens of  $\gamma$  titanium aluminide alloys suffer from temperature-induced damage when they are prepared solely by focused Ga ions. Such difficulties can be avoided by the suggested procedure that comprises focused Ga ion sputtering and final Ar ion polishing. Although the procedure is intricate and time-consuming it leads to large electron-transparent areas beneficial to convincing microstructural analysis, thereby representing a feasible alternative to the conventional preparation techniques like electro-polishing or sole Ar ion milling, which are generally not suited for the carefully targeted preparation of specimens.

The procedure was developed for  $\gamma$  titanium aluminides but might be also useful for other materials when considering their specific properties. The temperature rises during Ga ion sputtering are inversely proportional to the respective thermal conductivities. That is, materials with low thermal conductivities require generally more cautious approaches than materials with high thermal conductivities. The thermal conductivities of titan and steel are, for example, similar to the thermal conductivity  $\kappa = 24.2 \text{ W/(m}\cdot\text{K)}$  of the  $\gamma$  titanium aluminides so that they can be treated in the same fashion. In contrast, aluminium can be treated with more powerful Ga ion beams down to smaller specimen thicknesses prior to the final Ar ion polishing, because the thermal conductivity  $\kappa = 430 \text{ W/(m}\cdot\text{K)}$  is much larger. For materials with small thermal conductivities around  $\kappa = 1 \text{ W/(m}\cdot\text{K)}$  like silicon dioxide, finally, Ga beams with little power must be used leaving the specimens relatively thick when realising that temperature rises of several hundred °C are accessible even for specimens with large dimensions.

## Acknowledgements

The authors would like to thank M. Oehring, F. Pyczak, J.D.H. Paul, D. Matthiessen, and U. Lorenz for helpful discussions and support. They would also like to thank the referees for their valuable comments.

## References

- [1] J. Mayer, L.A. Giannuzzi, T. Kamino, and J. Michael, *TEM sample preparation and FIB-induced damage*, in *Focused Ion Beam Microscopy and Micromachining*, C.A. Volkert and A.M. Minor, eds., MRS Bull. Vol. 32, USA, 2007, pp. 400-407.
- [2] C.A. Volkert and A.M. Minor, *Focused ion beam microscopy and micromachining*, in *Focused Ion Beam Microscopy and Micromachining*, C.A. Volkert and A.M. Minor, eds., MRS Bull. Vol. 32, USA, 2007, pp. 389-399.
- [3] T. Ishitani and H. Kaga, *Calculation of local temperature rise in focused-ion-beam sample preparation*, J. Electron Microscopy. 44 (1995), pp. 331-336.
- [4] F. Appel, M. Oehring, and R. Wagner, *Novel design concepts for gamma-base titanium aluminide alloys*, Intermetallics 8 (2000), pp. 1283-1312.
- [5] F. Appel, M. Oehring, J. D.H. Paul, C. Klinkenberg, and T. Carneiro, *Physical aspects of hot-working gamma-based titanium aluminides*, Intermetallics 12 (2004), pp. 791-802.
- [6] U. Froebel and F. Appel, *Hot-workability of gamma-based TiAl alloys during severe torsional deformation*, Metall. Mater. Trans. A 38A (2007), pp. 1817-1832.
- [7] U. Froebel and A. Stark, *Microstructural evolution in gamma titanium aluminides during severe hot-working*, Metall. Mater. Trans. A 46A (2015), pp. 439-455.

- [8] A. Denquin and S. Naka, *Phase transformation mechanisms involved in two-phase TiAl-based alloys-II. Discontinuous coarsening and massive-type transformation*, Acta Mater. 44 (1996), pp. 343-352.
- [9] P. Shang, T.T. Cheng, and M. Aindow, *A high-resolution electron microscopy study on lamellar  $\gamma/\alpha_2$  interfaces in a low misfit TiAl-based alloy*, Philos. Mag. A 10 (1999), pp. 2553-2575.
- [10] M. J. Blackburn, *Some aspects of phase transformations in titanium alloys*, in *The Science, Technology, and Applications of Titanium*, R. Jaffee and N. E. Promisel, eds., Pergamon Press, New York, USA, 1970, pp. 633-664.
- [11] D.B. Williams, C.B. Carter, *Transmission Electron Microscopy*, Springer, New York, USA, 1996.
- [12] F.C. Frank and J.H. Van Der Merve, *One-dimensional dislocations. II. Misfitting monolayers and oriented overgrowth*, Proc. Roy. Soc. 198A (1949), pp. 216-225.
- [13] L.A. Giannuzzi and F.A. Stevie, *Introduction to Focused Ion Beams*, Springer, Boston, MA, USA, 2005.
- [14] J.F. Ziegler, J.P. Biersack, and U. Littmark, *The Stopping Range of Ions in Solids*, Pergamon Press, New York, USA, 1985.
- [15] M. Ohring, *Materials Science of Thin Films*, Academic Press, San Diego, USA, 2002.
- [16] U.R. Kattner, J.-C. Lin, and Y.A. Chang, *Thermodynamic assessment and calculation of the Ti-Al system*, Metall. Trans. A 23A (1992), pp. 2081-2090.
- [17] C. L. Fu, M. H. Yoo, *Elastic constants, fault energies, and dislocation reactions in TiAl: A first-principles total-energy investigation*, Philos. Mag. Lett. 62 (1990), pp. 159-165.
- [18] F. Appel, *Atomic level observations of mechanical damage in shot peened TiAl*, Philos. Mag. 93 (2013), pp. 2-21.
- [19] N. I. Kato, *Reducing focused ion beam damage to transmission electron microscopy samples*, J. Electron Microscopy 53(5) (2004), pp. 451-458.
- [20] J. P. McCaffrey, M. V. Phaneuf, and L. D. Madson, *Surface damage formation during ion-beam thinning of samples for transmission electron microscopy*, Ultramicroscopy 87 (2001), pp. 97-104.
- [21] C. J. Rossouw, C. T. Forwood, M. A. Gibson, and P. R. Miller, *Zone-axis convergent-beam electron diffraction and ALCHEMI analysis of Ti-Al alloys with ternary additions*, Philos. Mag. A 74 (1996), pp. 77-102.
- [22] J. L. Murray, *Pt-Ti (Platinum-Titanium) in Binary Alloy Phase Diagrams*, second ed., T. B. Massalski, H. Okamoto, P. R. Subramanian, and L. Kacprzak, eds., Am. Soc. Metals Vol. 3, Ohio, USA, 1992, pp. 3141-3143.
- [23] Y. Mishin and C. Herzig, *Diffusion in the Ti-Al system*, Acta Mater. 48 (2000), pp. 589-623.
- [24] R. Banerjee, S. Swaminathan, R. Wheeler, and H. L. Fraser, *Phase evolution during crystallization of amorphous titanium aluminide thin films: Effect Mn and Nb additions*, in *Metastable Phases and Microstructures*, R. Bormann, G. Mazzone, R. D. Shull, R. D. Averback, and R. F. Ziolo, eds., MRS Symp. Proc. Vol. 400, Pittsburgh, PA, USA, 1996, pp. 215-220.
- [25] H. S. Carslaw and J. C. Jaeger, *Conduction of Heat in Solids*, second ed., Oxford University Press, Oxford, UK, 1959.
- [26] F. Appel, J. D. H. Paul, and M. Oehring, *Gamma Titanium Aluminide Alloys*, Wiley-VCH Verlag & Co. KGaA, Weinheim, 2011.
- [27] L. A. Giannuzzi, R. Geurts, and J. Ringnalda, *2 keV Ga<sup>+</sup> FIB milling for reducing amorphous damage in silicon*, Microscopy and Microanalysis 11 suppl. 2 (2005), pp. 828-829.

- [28] D. Bahnck and R. Hull, *Experimental measurement of transmission electron microscope specimen temperature during ion milling*, in *Specimen Preparation for Transmission Electron Microscopy of Materials II*, R. Anderson, ed., MRS Symp. Proc. Vol. 199, Pittsburgh, PA, USA, 1990, pp. 253-261.
- [29] J. Orloff, M. Utlaut, and L. Swanson, *High Resolution Focused Ion Beams: FIB and its Applications*, first ed., Kluwer Academic/Plenum Publishers, New York, USA, 2003.
- [30] M. Schaffer, B. Schaffer, and Q. Ramasse, *Sample preparation for atomic-resolution STEM at low voltages by FIB*, *Ultramicroscopy* 114 (2012), pp. 62-71.
- [31] E. Chason and M. J. Aziz, *Spontaneous formation of patterns on sputtered surfaces*, *Scripta Mater.* 49 (2003), pp. 953-959.

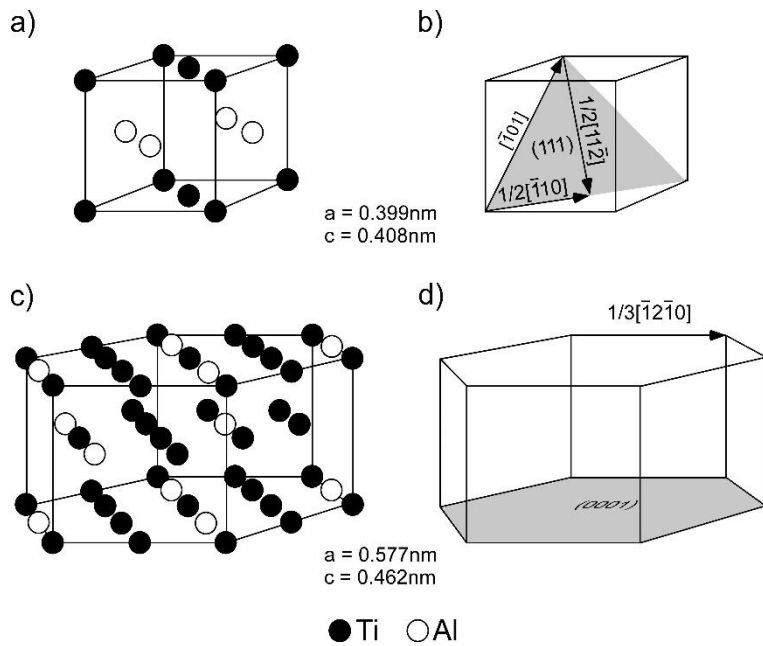


Figure 1. Atomic arrangements of the  $\gamma$ (TiAl) and  $\alpha_2$ (Ti<sub>3</sub>Al) phases as well as the Burgers vectors of the  $\gamma$  phase. a) Ordered tetragonal L1<sub>0</sub> structure of the  $\gamma$  phase. b) Burgers vectors of ordinary  $1/2\langle \bar{1}10 \rangle$  dislocations as well as  $\langle \bar{1}01 \rangle$  and  $\langle 11\bar{2} \rangle$  superdislocations in  $\gamma$ . The superdislocations are necessary to maintain the atomic order when shear components in the c direction are involved. The (111) plane is indicated. c) Ordered hexagonal D0<sub>19</sub> structure of  $\alpha_2$ . d) The  $[\bar{1}2\bar{1}0]$  direction and the (0001) plane are indicated in  $\alpha_2$ .

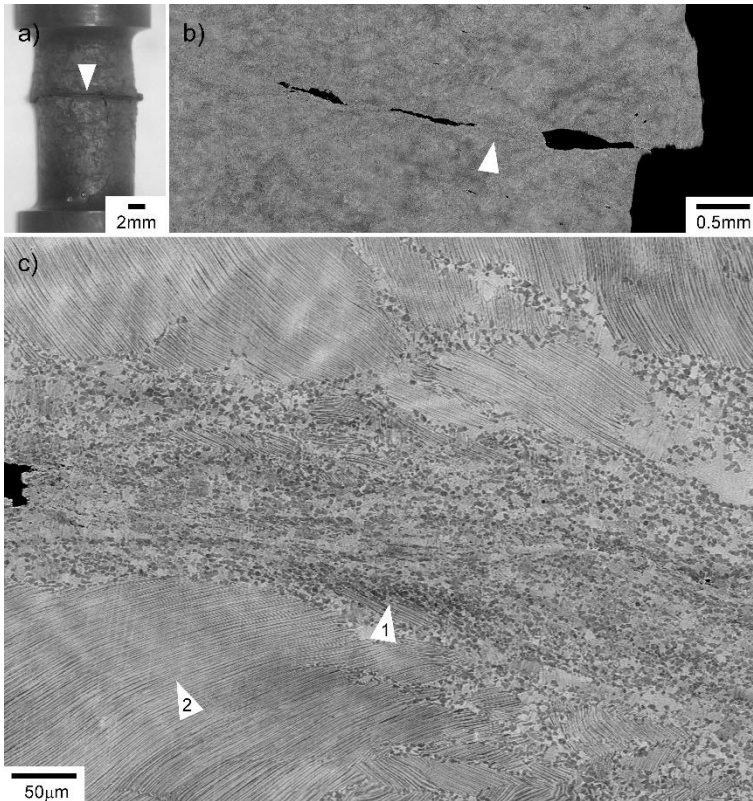


Figure 2. Shear localization and crack formation during severe torsional deformation combined with compression. a) A crack was formed in the central region of the sample (arrow) during hot-working. b) Back-scattered electron (BSE) image of the crack (marked by an arrow in a)) in the longitudinal section of the sample through the sample axis. c) Detail of b) marked there by an arrow, revealing a narrow shear band (arrow 1), which originally transversed the cross section of the sample, but which in the course of deformation has also partly separated and has given rise to cracking. The shear band is embedded in lamellar colonies (arrow 2), the main structural constituent of the alloys after casting. Furthermore, the phase components  $\gamma$  and  $\alpha_2$  appear dark and bright respectively, under the BSE imaging conditions. Ti-45Al-8Nb, hot-working temperature  $T = 1200^\circ\text{C}$ , torsional shear strain  $\Phi_T$  (torsion reversed after  $1/4$  revolution) = 12.64 which conforms to the effective strain  $\bar{\epsilon} = 7.3$ , effective strain rate  $d\bar{\epsilon}/dt = 1 \cdot 10^{-2} \text{s}^{-1}$ , and compressive strain  $\epsilon = 0.06$ .

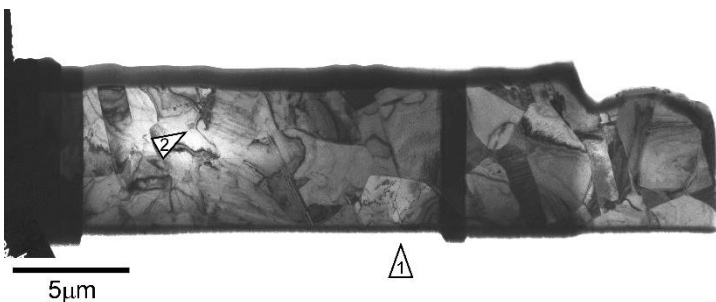
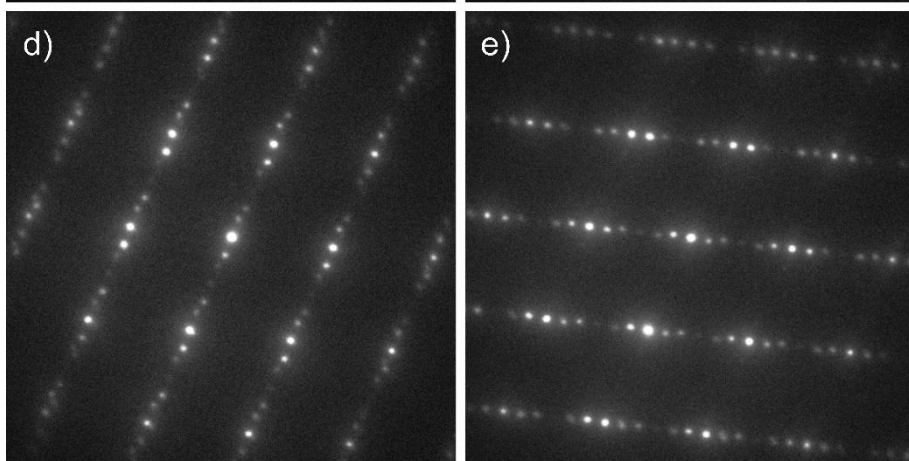
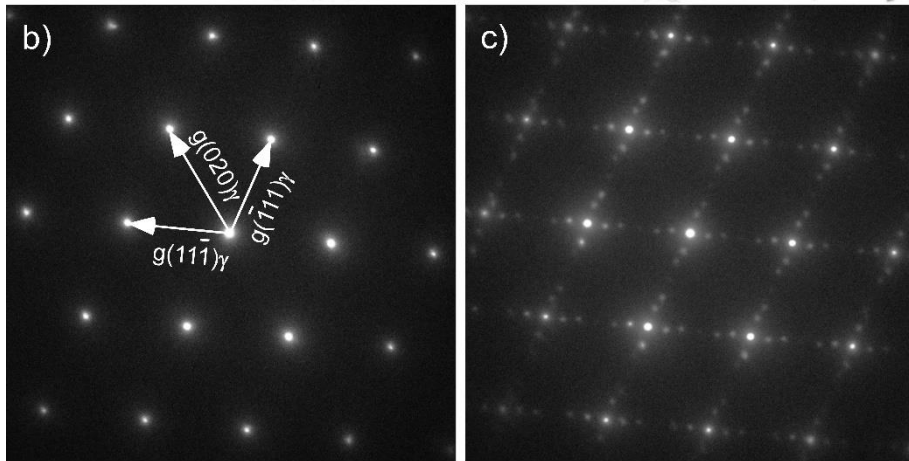
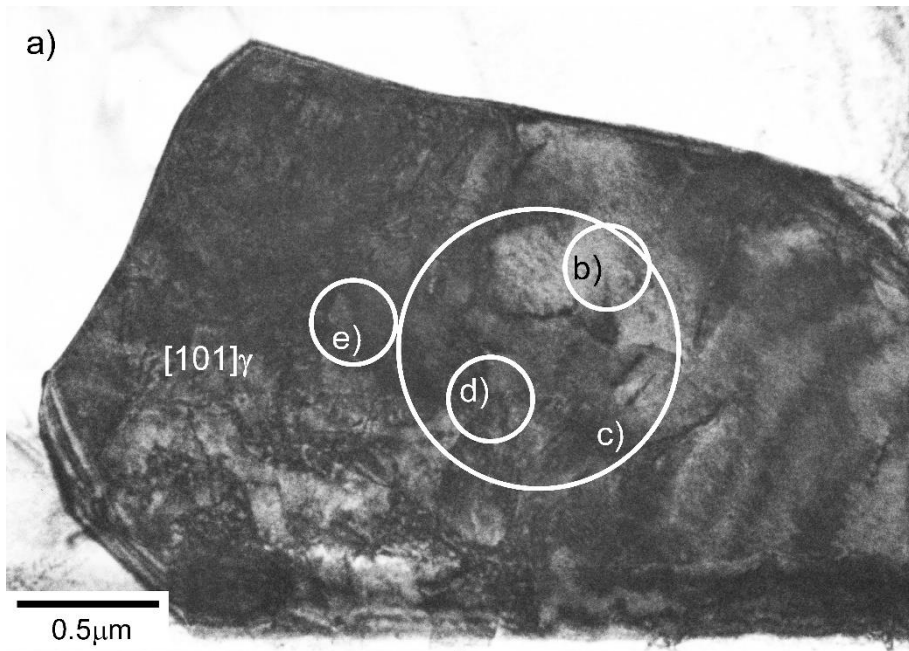


Figure 3. Specimen solely prepared by Ga ions. The TEM bright field (BF) image depicts the recrystallized microstructure of a shear band. The upper horizontal and dark-appearing fringe is a remnant of a Pt layer, which was deposited onto the specimen at the very beginning of the preparation process by the gas injection system (GIS) using the Ga beam to reduce the curtaining effect during polishing. The dark vertical ribbon to the right of the  $\gamma$  grain being marked by arrow 1 denotes a region that was left blank during polishing so that it is not transparent for electrons. Ti-46.5Al-5Nb.



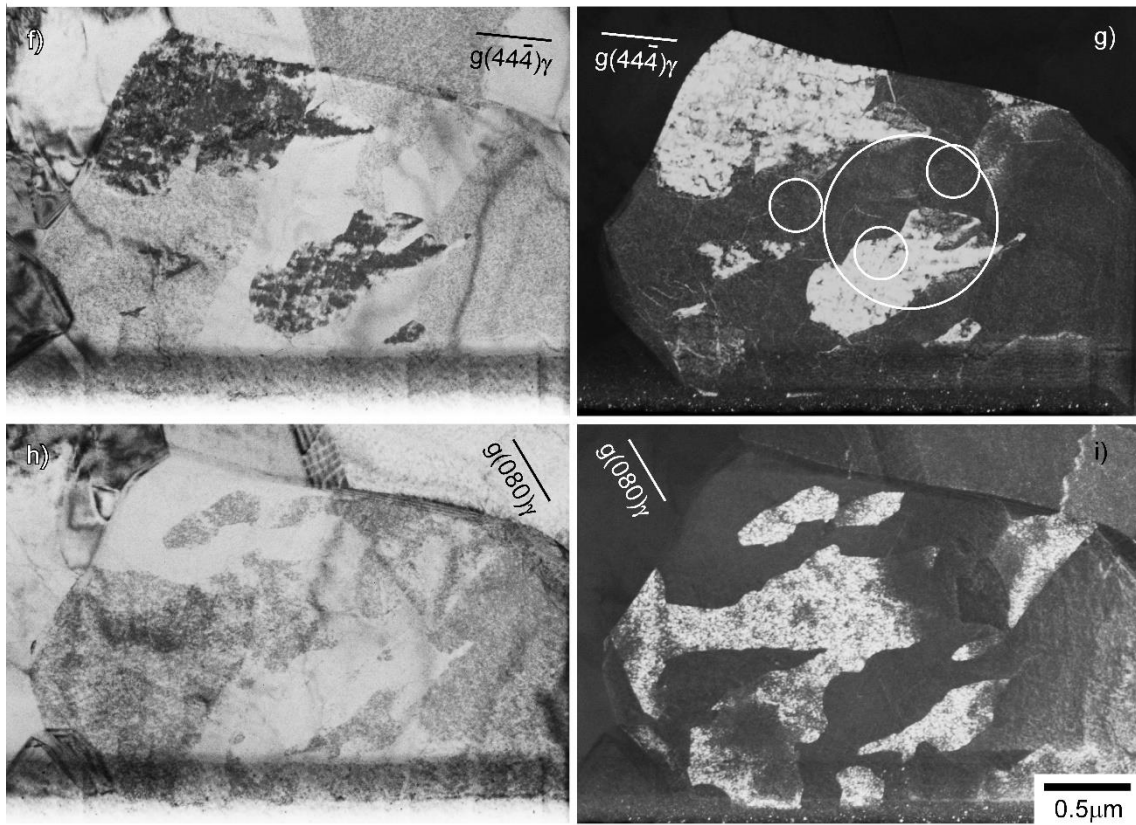


Figure 4. Specimen damage after preparation with Ga ions. a) The TEM BF image indicates the  $\gamma$  grain, which is marked in Figure 3 by arrow 1, in  $[101]\gamma$  orientation. b) The related diffraction pattern of the  $[101]\gamma$  zone axis. The associated position and size of the projected SAD aperture is depicted in a) by the white circle marked correspondingly. The aperture has a diameter of  $10\mu\text{m}$ . In addition the three shortest reciprocal lattice vectors are displayed. c) Diffraction pattern that results when using a SAD aperture with a diameter of  $40\mu\text{m}$ . d) The variant 1 diffraction pattern. e) The variant 2 diffraction pattern. f) BF recording indicating the grain when imaged with the reciprocal lattice vector depicted. g) The related DF recording. The positions and sizes of the projected SAD apertures from a) are shown once again. h) and i) BF and DF images under a different contrast condition. Ti-46.5Al-5Nb.

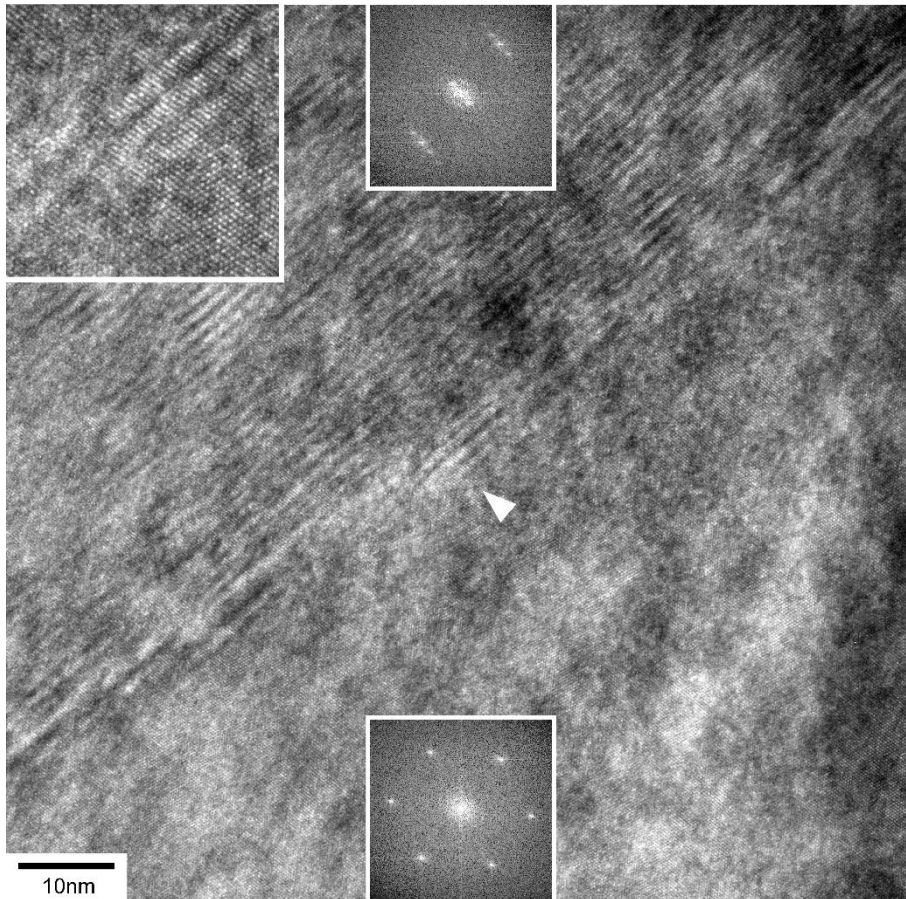


Figure 5. Edge of a crystal platelet. The HRTEM image was recorded in the region, which is marked in Figure 3 by arrow 2 and shows the crystal structure of the  $\gamma$  phase in  $[101]\gamma$  orientation. The associated fast Fourier transform (FFT) is displayed in the insert at the bottom edge. The upper part depicts a Moiré pattern resulting from the coating with a crystal platelet. The platelet is of the variant 1 type, which is revealed by the related FFT displayed in the insert at the centre of the upper edge. The FFT also indicates that this part is tilted slightly out of the zone axis position. Finally, the third insert shows the central transition region marked by an arrow. Ti-46.5Al-5Nb.

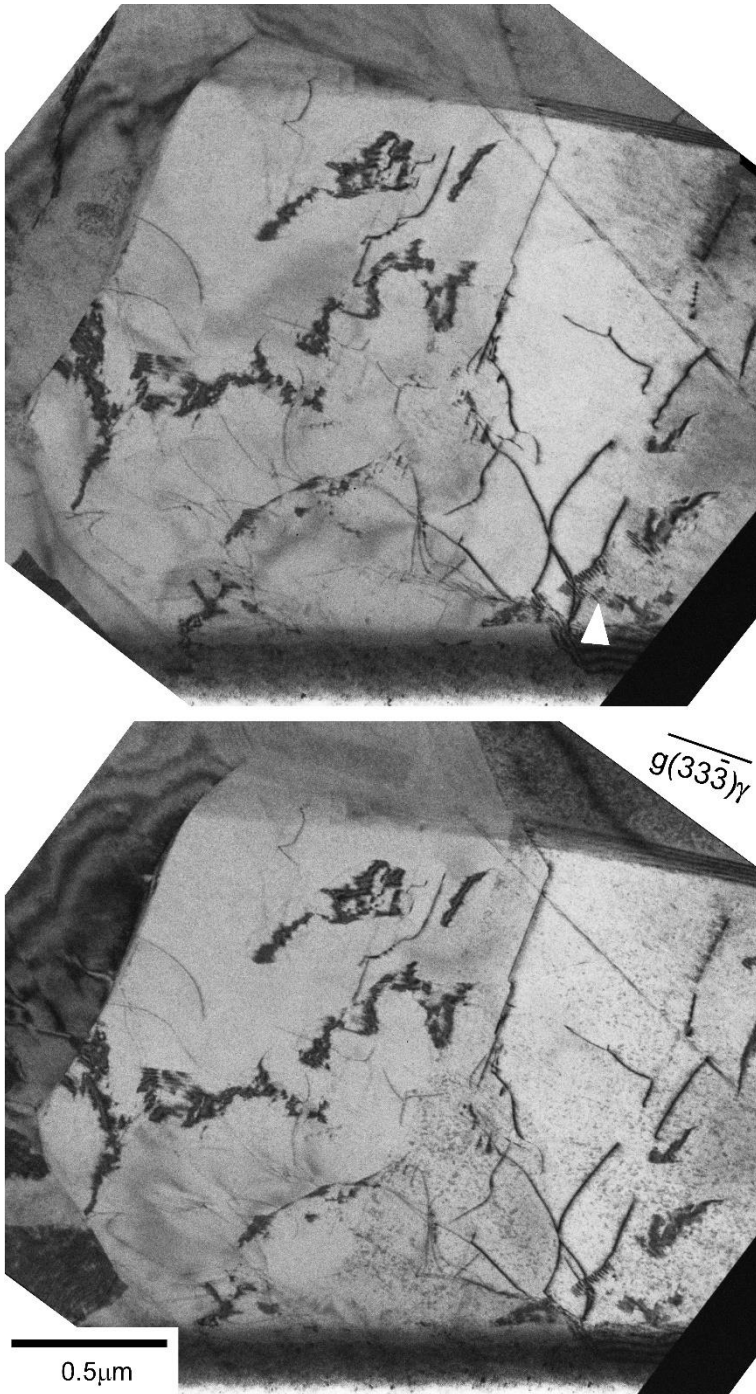


Figure 6. Stereographic image. It reveals that the dark and streaky areas (arrow) are located exclusively at the specimen surfaces indicating that they are manifestations of the Moiré contrast. Ti-46.5Al-5Nb.

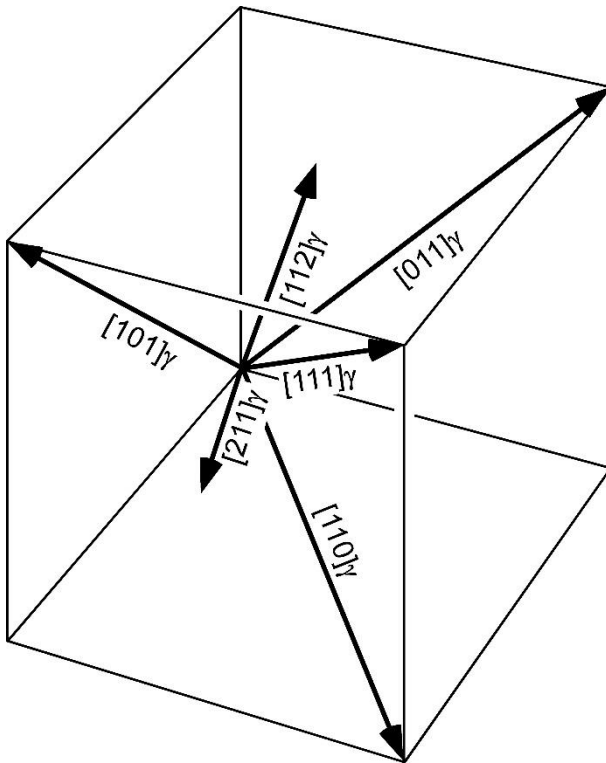


Figure 7. Zone axes being analysed. In addition to the  $[101]_{\gamma}$  zone axis, the zone axes  $[011]_{\gamma}$ ,  $[110]_{\gamma}$ ,  $[111]_{\gamma}$ ,  $[112]_{\gamma}$ , and  $[211]_{\gamma}$  were examined to be able to identify the platelet phase.

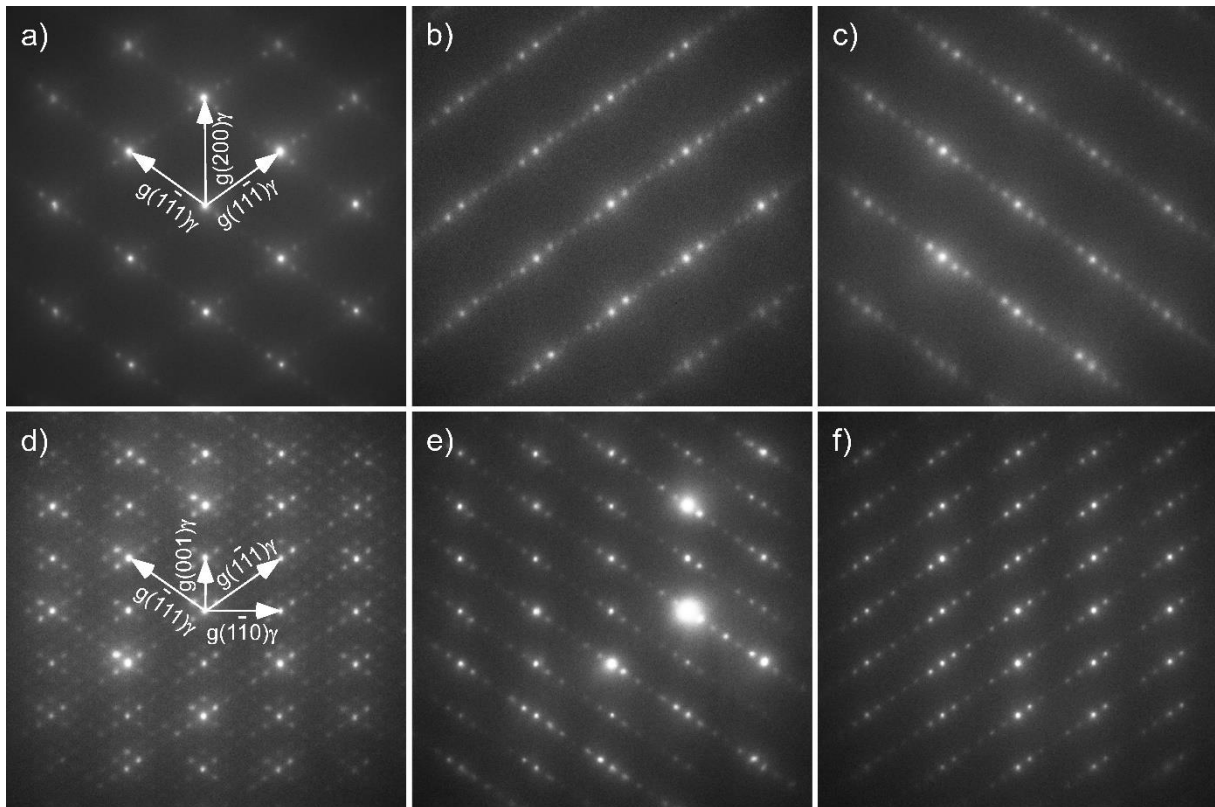


Figure 8. Diffraction patterns of the  $[011]\gamma$  and  $[110]\gamma$  zone axes. a) Diffraction pattern of the  $[011]\gamma$  zone axis. The three shortest reciprocal lattice vectors of the  $\gamma$  phase are displayed. b) The variant 2 pattern of the  $[011]\gamma$  zone axis. c) The variant 3 pattern of the  $[011]\gamma$  zone axis. d) Diffraction pattern of the  $[110]\gamma$  zone axis. The four shortest reciprocal lattice vectors of the  $\gamma$  phase are displayed. e) The variant 1 pattern of the  $[110]\gamma$  zone axis. f) The variant 3 pattern of the  $[110]\gamma$  zone axis. Ti-46.5Al-5Nb.



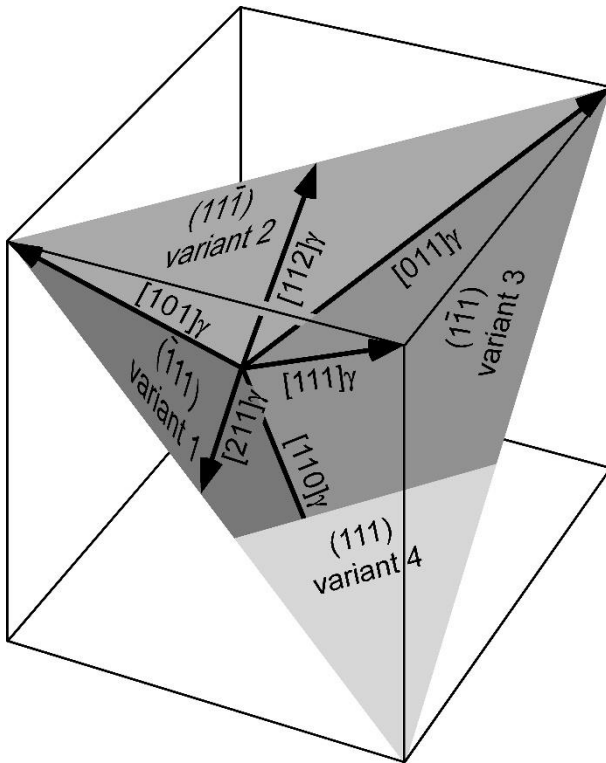


Figure 10. Orientation of the four crystal platelet variants with respect to the  $\gamma$  phase. The  $(0002)\alpha$  plane of each platelet is oriented parallel to one of the four  $\{111\}\gamma$  planes so that, all in all, four different platelet variants result. From these four variants always only two are detectable when viewing along the  $[101]\gamma$ ,  $[011]\gamma$ , or  $[110]\gamma$  zone axis.

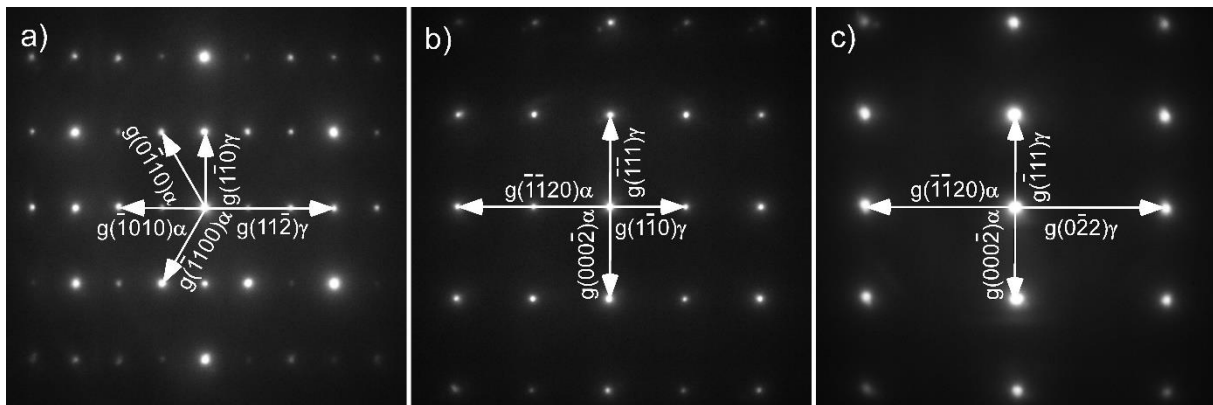


Figure 11. Diffraction patterns of the  $[111]\gamma$ ,  $[112]\gamma$ , and  $[211]\gamma$  zone axes. a)  $[111]\gamma$  zone axis. Depicted are two  $\gamma$  lattice vectors of the  $[111]\gamma$  and three of the  $[0001]\alpha$  zone axis. The spots, which do not belong to  $\gamma$  or  $\alpha$  are double diffraction spots. b)  $[112]\gamma$  zone axis with always two reciprocal lattice vectors of the  $[112]\gamma$  and  $[\bar{1}100]\alpha$  zone axis. c)  $[211]\gamma$  zone axis with always two reciprocal lattice vectors of the  $[211]\gamma$  and  $[\bar{1}100]\alpha$  zone axis. Ti-46.5Al-5Nb.

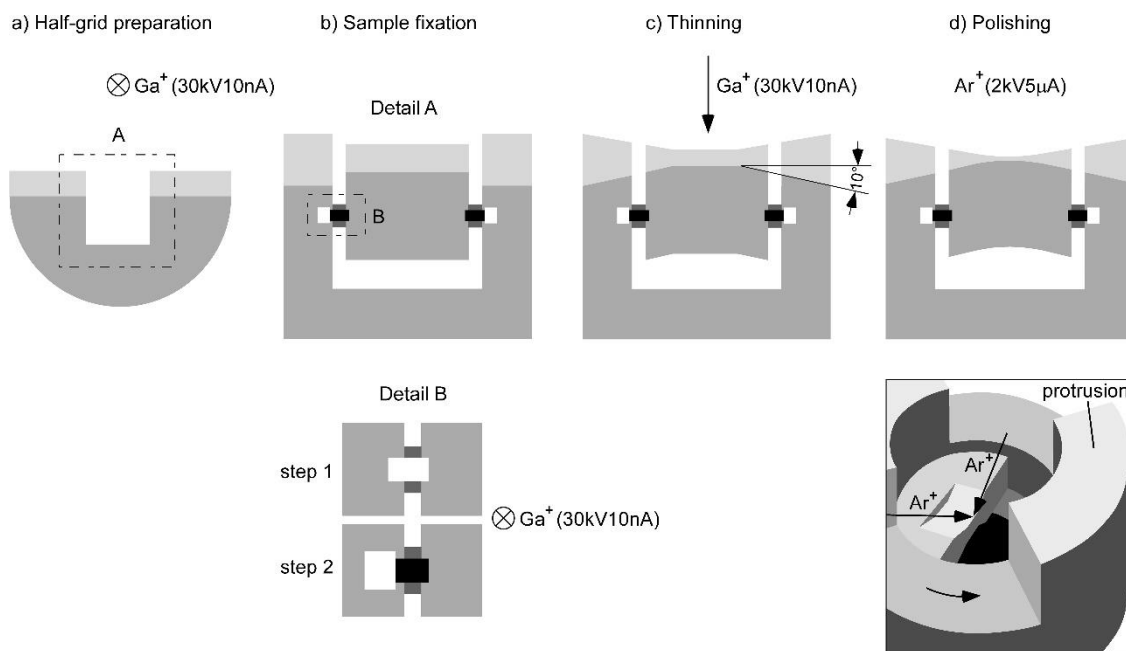


Figure 12. Specimen preparation with Ga and Ar ions. The preparation takes place in four steps. a) Preparation of the half-grid. Most of the work is done conventionally by cutting and grinding. Only the notch incorporating the specimen is formed by a 30kV10nA Ga ion beam using the deposition mode. For this purpose the grid is tilted in such a way that the beam impinges under an angle of  $39^\circ$ . The beam direction points vertically into the image plane as indicated by the quartered circle, so that it is also the viewing direction making the side and brighter top side of the grid visible simultaneously. b) Fixation of the specimen occurs in two steps using the same settings as in a). During the first step the beam is confined to a rectangular window, which covers the edges of both the specimen and grid. The sputtered material is partially deposited in the gaps lying in between, thereby to some extent filling them up gradually, with the depositions depicted in dark grey. Subsequently, during the second step, the window is situated entirely within the grid with a small overlap to the first window. The sputtering then fills up the region of the first window, which is now depicted in black, thereby strengthening the connection. c) Thinning with a 30kV10nA Ga ion beam parallel to the grid using the mill-for-depth mode. The beam is confined to a trapezoid-shaped window that leaves the ends of the specimen thicker. Furthermore, the inclination angle of  $10^\circ$  makes sure that the Ar ion beam is not shadowed by the specimen in any way. d) Polishing with a 2kV5µA Ar ion beam under an angle of  $10^\circ$ . Both Ar sources are directed towards the top specimen side so that the grid must be turned over to polish the specimen on the underside. Finally, the holder rotates with 6 revolutions per minute, with the beam sectionally blanked by the two protrusions.

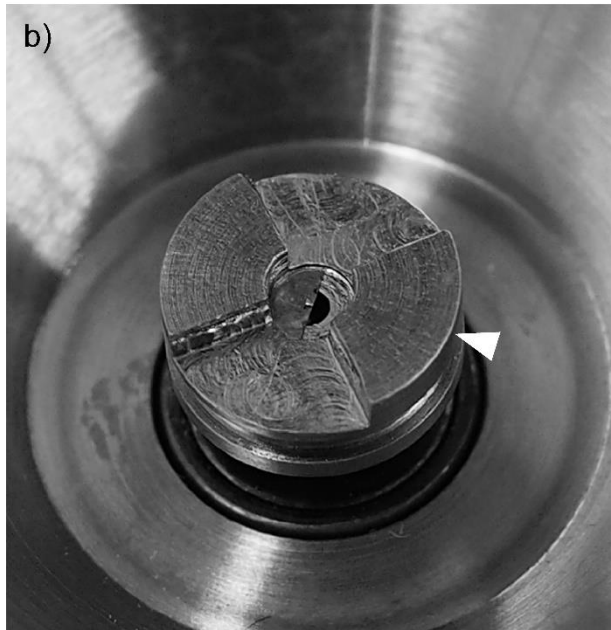
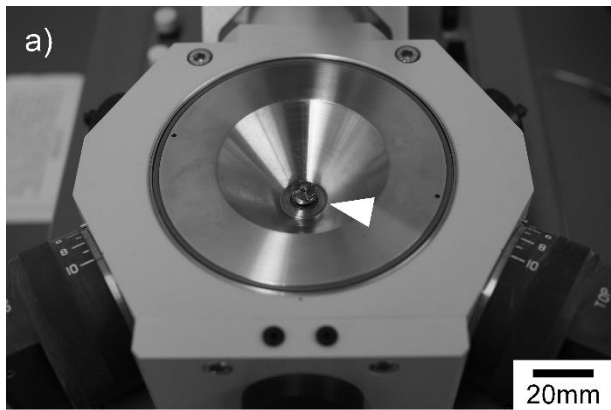


Figure 13. Design of the Ti-holder. a) The holder is marked by an arrow. It is attached to the piston of the PIPS, which is situated in the airlock. After evacuation, it is moved down into the main working chamber for the Ar ion treatment, with the casings of the guns visible in the lower image corners. b) The grid is mounted onto the holder in the way depicted, in order to effectively protect the connections with the specimen by the protrusions (arrow) against ion beam damage.

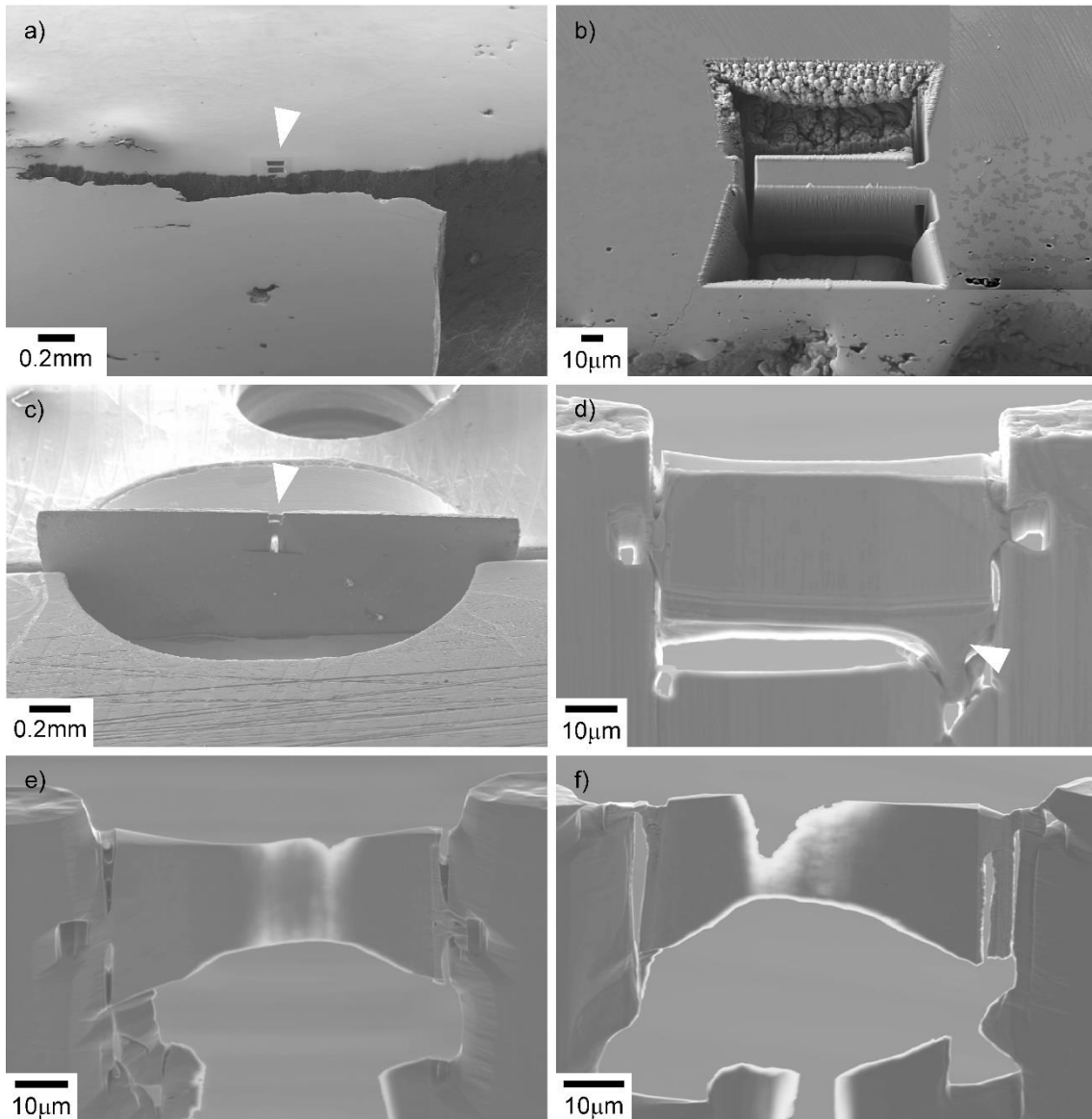


Figure 14. Illustration of the various stages of specimen preparation. a) The SEM image shows a specimen withdrawal position (arrow) at a crack wake being recorded with secondary electrons (SE). b) High magnification image of the withdrawal position marked in a) by the arrow. It shows the specimen shape immediately before lift-out. Please note that the specimen is more than  $15\mu\text{m}$  thick in this stage in order to ensure a good heat transfer. The image contrast is low because the SE technique is not sensitive with respect to compositional changes. Therefore, the contrast was enhanced electronically at the right image edge to indicate the transition zone between the finely recrystallized shear band and the original lamellar structure. c) The specimen (arrow) is positioned in the half grid and already thinned, with the grid being approximately  $40\mu\text{m}$  thick. d) High magnification image of the specimen marked in c), which is about  $6\mu\text{m}$  thick in the central region. The image clearly indicates the connections between the specimen and the grid. The connection zones sideways from the holes towards the specimen correspond to the black rectangles in Figure 12, whereas the regions between the specimen and the grid immediately above and beneath these zones correspond to the rectangles in dark grey. The redeposited material beneath the specimen, which is marked by an arrow, stems from preliminary pinning processes. They were sometimes conducted prior to the final pinning to be able to quickly separate the manipulator needle from the specimen in order to avoid any damage, which may be caused by the drift of parts of the instrument. This final pinning can last hours depending on the specimen thickness before thinning. e) Specimen shape after the final

polishing. The image was recorded at an acceleration voltage of 6kV. f) A second specimen, which was also recorded at 6kV. The specimen surfaces were turned as little as  $1.5^\circ$  into the beam during thinning in contrast to the surfaces of the previous specimen, which were turned by  $2^\circ$ . The smaller tilt angles led to a wedge-shaped cross-section and, eventually, a partial dissolution of the upper specimen regions during the final polishing. The top side of the specimen was initially coated with a Pt layer. This is in contrast to the previous specimen, which was not coated. It turned out that specimens without Pt layers have also smooth surfaces after the final polishing, due to the rotation of the grids levelling out irregularities developed during thinning, so that coatings are dispensable. Furthermore, a big portion of the connections was dissolved during polishing, so that only remnants remained at the top side. Ti-45Al-5Nb.

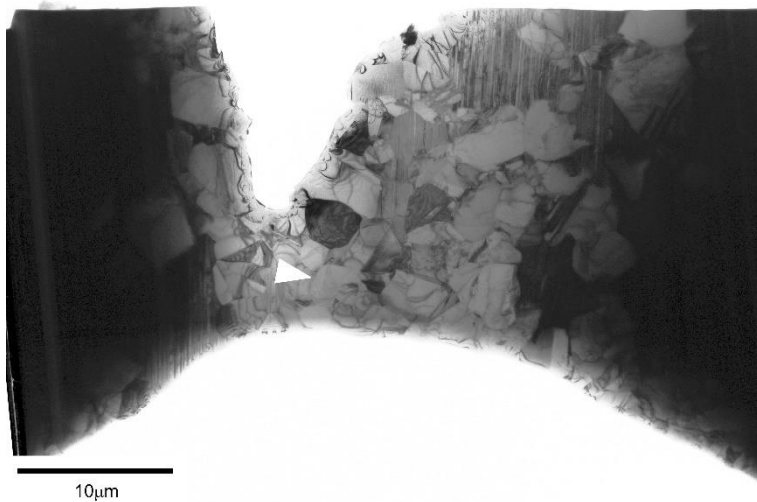
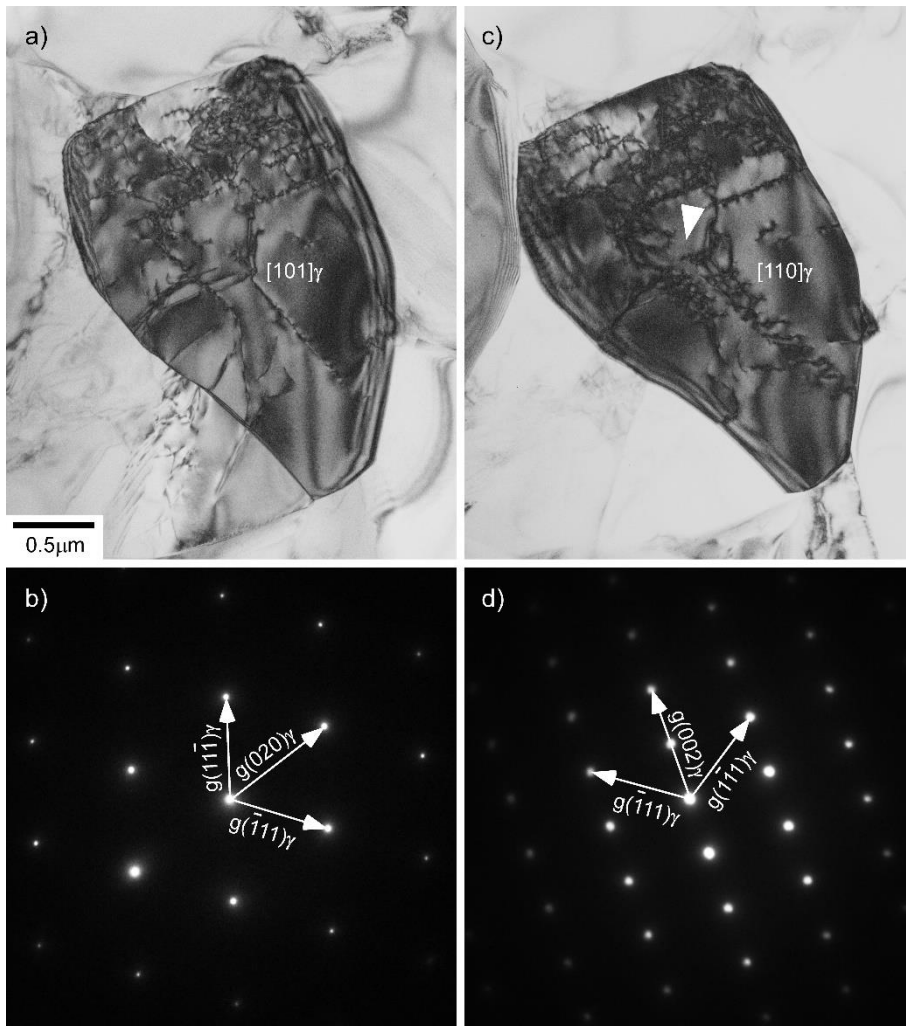


Figure 15. Specimen after preparation with Ga and Ar ions. The TEM BF image shows the entire electron transparent area of the specimen, which is depicted in Figure 14 f). There are no remnants of the Pt layer present any more on the top side of the specimen revealing that the layer was completely sputtered in this area during polishing. This is comprehensible when realising that the Ar ion beams impinge in the process also upon the entire top side of the specimen (Figure 12d)). Ti-45Al-5Nb.



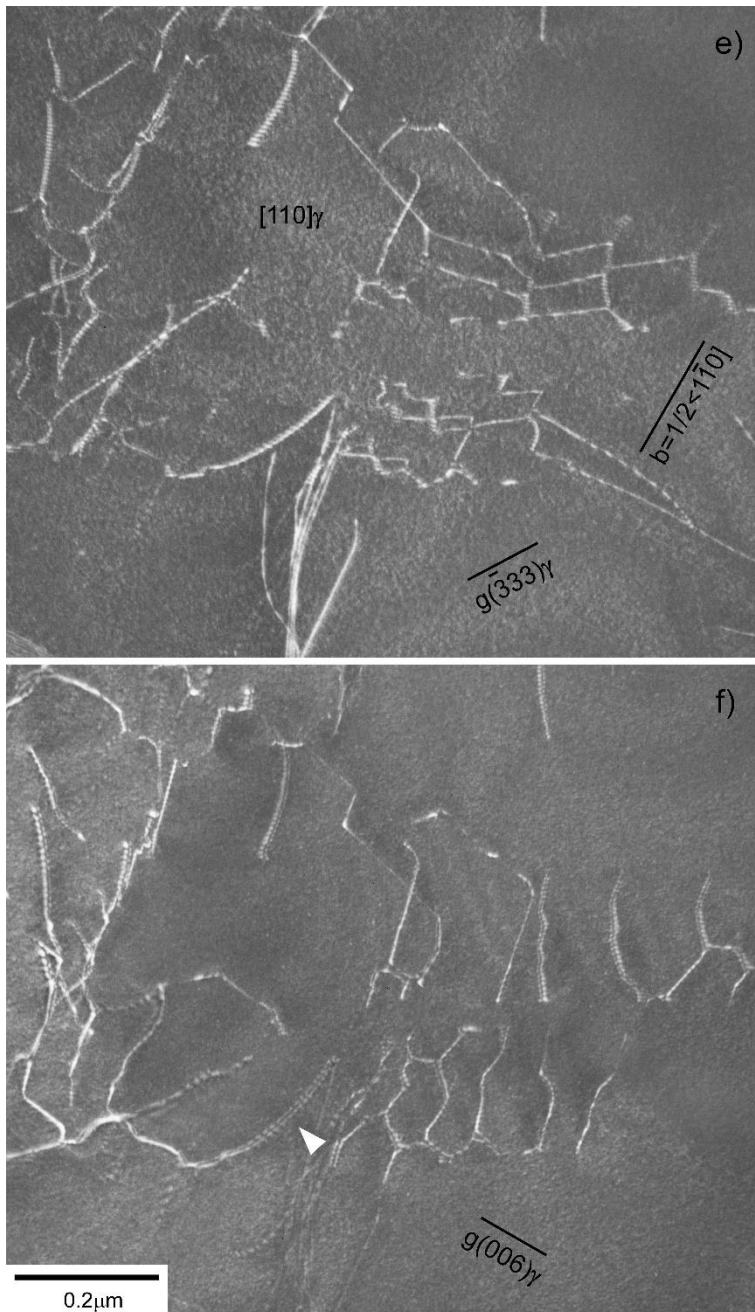


Figure 16. Specimen after preparation with Ga and Ar ions. a) The  $\gamma$  grain, which is marked in Figure 15 by an arrow, is depicted in  $[101]_{\gamma}$  orientation. b) The related  $[101]_{\gamma}$  zone axis diffraction pattern. c) Recording of the grain when tilted into the  $[110]_{\gamma}$  orientation. d) The related  $[110]_{\gamma}$  zone axis diffraction pattern. e) and f) The WB DF images show the central region of the grain, which is marked in c) by an arrow, under two different diffraction conditions. The vector  $g(\bar{3}33)_{\gamma}$  (e) displays ordinary  $\frac{1}{2}\langle 1\bar{1}0 \rangle$  dislocations as well as superdislocations whereas the vector  $g(006)_{\gamma}$  (f) displays solely superdislocations. The dissociation of the superdislocations into partials is clearly recognisable in f) (arrow). Ti-45Al-5Nb.